Progress In Electromagnetics Research C, Vol. 124, 197–209, 2022

Deep-Learning Linear Sampling Method for Shape Restoration of Multilayered Scatterers

Yu-Hsin Kuo and Jean-Fu Kiang*

Abstract—A deep learning linear sampling method (DLSM), composed of linear sampling method (LSM) and a convolutional neural network (CNN) of U-Net, is proposed to restore shape of multilayered scatterers with cylindrical or rectangular cross section. Simulations over random samples with different geometrical parameters are used to verify the efficacy of the proposed method.

1. INTRODUCTION

Various types of inverse scattering problem (ISP) have been developed to retrieve object shape and properties from the scattering fields in surveillance [1], medical diagnosis [2], and geographical exploration [3]. The formulations are usually ill-posed and require some prior knowledge or constraints to acquire the solutions [4]. Linear sampling method (LSM) has been used for restoring object shape [5, 6], by solving linear equations at each pixel in a detection domain, without resorting to nonlinear optimization techniques [7]. An orthogonality sampling method (OSM) was proposed for shape reconstruction from the reduced scattering field computed using the Green's function [2, 8, 9]. Both LSM and OSM were based on an indicator function and required some empirical threshold.

In conventional LSMs, an empirical threshold was chosen to determine if a pixel belonged in an object [10], with no definite method on how to choose a proper threshold. In [10], a reference ball was artifically added to the detection domain, and a threshold was determined by trial-and-error on the restored image. In [11], an indicator function of LSM was proposed in terms of multipole expansion. The object shape was better restored by using only the monopole and dipole terms [4] than using conventional LSMs.

In [7], a phase-delay frequency variation (PDFV) method was proposed to highlight the object shape by using the phase information of LSM over multiple frequencies. The phases of LSM at different frequencies were related to the electrical length traversed by the incident wave from the transmitters to the pixel of interest. Some artifacts can be reduced by exploiting multiple frequencies, but an empirical threshold is still required.

Other than the threshold issue, it was observed that conventional LSM had difficulty in distinguishing solid cylinder from ring [6]. The modified LSM in [11] can distinguish a solid object from a hollow one, but an object surrounded with a rectangular wall could not be clearly restored.

Machine learning methods have been applied to solve ISPs. In [12], a supervised descent method (SDM) was applied to restore object shape and estimate its permittivity. It was found that multiple cylinders could be better restored if they were compared with prior models, while complicated shapes like T or solid-star could be better restored as a cluster of pixels. In [13], an U-Net [14] was applied in conjunction with three pixel-based methods, direct inversion scheme (DIS), backpropagation scheme (BPS) and dominant current scheme (DCS). The scattered fields in the DIS were used to estimate the permittivity profile, while BPS and DCS were used to generate preliminary inverse results as input to

Received 10 August 2022, Accepted 9 September 2022, Scheduled 25 September 2022
* Corresponding author: Jean-Fu Kiang (jfkiang@ntu.edu.tw).
The authors are with the Graduate Institute of Communication Engineering, National Taiwan University, Taipei 10617, Taiwan.

the U-Net. The DCS was claimed to perform better than subspace optimization methods in restoring shape and physical properties of an object.

In [15], ultrasound-acquired tissue properties were used as prior information for a contrast source inversion (CSI) technique. Then, the real part, imaginary part and magnitude of the acquired permittivity were used as input to the U-Net [14], which improved the accuracy of estimated permittivity and removed some artifacts in the ultrasound image.

In [16], a deep convolutional neural network (DConvNet) was applied to retrieve the permittivity distribution from the scattered fields, which was input to a deep residual convolutional neural network (DRCNN) to highlight the edges of high-contrast objects. In [3], an autoencoder was used to transform the permittivity distribution in a detection domain of 128×128 pixels to a vector of 256 elements, which were used to train a deep learning network (DLN) in conjunction with the scattered fields. The autoencoder could well recover high-contrast objects with shapes of square, triangle or square enclosed by ring, which were otherwise restored as near-circular shape by using distorted Born iterative method or phase confocal method. In [17], a convolutional neural network (CNN) was combined with an iterative method to retrieve parameters of high-contrast or complicated objects. In [18], a U-Net was trained on regular images, with OSM indicators in the RGB channels as input. No threshold was needed as in conventional OSM, and two adjacent cylinders could be well distinguished with U-Net.

In this work, a deep learning linear sampling method (DLSM) is proposed to restore the shape of multilayered objects, with LSM indicator as input to a CNN for training and validation. No empirical threshold, as in conventional LSMs, is required to determine if a pixel belongs in an object. The efficacy of DLSM is demonstrated and verified with a variety of nested rectangles and nested circles, which are usually restored as solid rectangles and solid circles, respectively, if using conventional LSMs.

The rest of this paper is organized as follows. The formulations of ISP and LSM are briefly reviewed in Section 2. The proposed DLSM and U-Net are presented in Section 3. The training data set and performance indices are presented in Section 4. Simulation results are discussed in Section 5, and some conclusions are drawn in Section 6.

2. FORMULATION OF ISP AND LSM

Figure 1(a) shows a schematic of 2D scattering problem, with scatterers distributed within a 2D detection domain (D_d) encircled by M_e exciting probes and M_r receiving probes. The detection domain is divided into N_d uniform pixels. All the probes are placed on a circular perimeter (C_0) surrounding the detection domain, with exciting probes at $\bar{r}''_{m_e}$, with $1 \le m_e \le M_e$, and receiving probes at $\bar{r}_{m_r}$, with $1 \le m_r \le M_r$.

The scattering field at $\bar{r}$, attributed to the exciting probe at $\bar{r}''$, is given by

$$E_s(\bar{r}, \bar{r}'') = E_t(\bar{r}, \bar{r}'') - E_i(\bar{r}, \bar{r}'') = k_b^2 \iint_{D_d} G(\bar{r}, \bar{r}')\chi(\bar{r}')\bar{E}_t(\bar{r}', \bar{r}'')d\bar{r}' \tag{1}$$

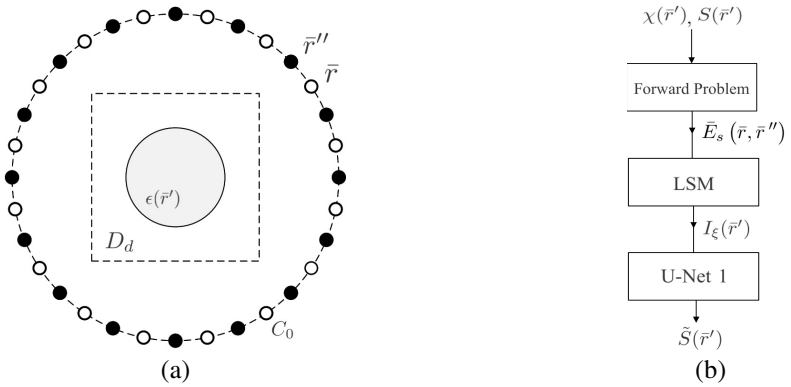

Figure 1. (a) Schematic of a 2D detection domain (embedding scatterers) encircled by M_e exciting probes (•) and M_r receiving probes (○). (b) Flow-chart of proposed deep learning linear sampling method (DLSM).

where $E_s(\bar{r},\bar{r}'')$, $E_t(\bar{r},\bar{r}'')$, and $E_i(\bar{r},\bar{r}'')$ are the scattering field, the total field, and the incident field, respectively, measured at $\bar{r}$; $k_b = \omega\sqrt{\mu_b\epsilon_b}$ is the wavenumber of the background medium, with permittivity ϵ_b and permeability μ_b,

$$\chi(\bar{r}') = \frac{\epsilon(\bar{r}') - \epsilon_b}{\epsilon_b} \tag{2}$$

is the contrast function, and $\epsilon(\bar{r}')$ is the permittivity at $\bar{r}' \in D_d$. The 2D Green's function, $G(\bar{r},\bar{r}')$, satisfies the wave equation

$$\left(\nabla^2 + k_b^2\right) G(\bar{r},\bar{r}') = -\delta(\bar{r} - \bar{r}') \tag{3}$$

and has the explicit form of

$$G(\bar{r},\bar{r}') = -\frac{j}{4} H_0^{(2)}(k_b|\bar{r} - \bar{r}'|) \tag{4}$$

where $H_0^{(2)}$ is the zeroth-order Hankel's function of the second kind.

An inverse problem is formed by using $E_s(\bar{r},\bar{r}'')$ to estimate $\epsilon(\bar{r}')$ and thus restoring the scatterer shape in D_d as a by-product. An adjoint equation is formulated as [19, 20]

$$\int_{C_0} E_s(\bar{r},\bar{r}'')\xi(\bar{r}',\bar{r}'')d\bar{r}'' = G(\bar{r},\bar{r}') \tag{5}$$

where $\xi(\bar{r}',\bar{r}'')$ is an adjoint field. The contour integral over C_0 in (5) can be approximated as a weighted sum over all the exciting probes as

$$\sum_{m_e=1}^{M_e} \zeta_{m_e} E_s(\bar{r},\bar{r}''_{m_e})\xi(\bar{r}',\bar{r}''_{m_e}) = G(\bar{r},\bar{r}') \tag{6}$$

where ζ_{m_e} is the weighting factor assigned to the m_eth exciting probe. By taking samples of (6) over the detection domain, at $\bar{r}' = \bar{r}'_{n_d}$, with $1 \le n_d \le N_d$, a matrix equation is formed as [5]

$$\bar{\bar{A}} \cdot \bar{f} = \bar{g} \tag{7}$$

where

$$\begin{aligned} A_{m_r m_e} &= \zeta_{m_e} E_s(\bar{r}_{m_r},\bar{r}''_{m_e}), \\ f_{m_e} &= \xi(\bar{r}'_{n_d},\bar{r}''_{m_e}), \\ g_{m_r} &= G(\bar{r}_{m_r},\bar{r}'_{n_d}) \end{aligned} \tag{8}$$

with $1 \le m_e \le M_e$ and $1 \le m_r \le M_r$. Eq. (7) is then solved to obtain $\bar{f}$ by using the singular-value decomposition (SVD) and the Tikhonov regularization techniques.

In this work, we choose the minimum eigenvalue of $\bar{\bar{A}}$ as the Tikhonov parameter in the SVD, reducing the burden of finding an empirical Tikhonov parameter. To test the robustness of this approach under noise, Gaussian random noise with variance δ_g^2 is added to E_s of each receiving probe, in the testing data set, with $\delta_g^2 = \langle\|E_s\|^2\rangle 10^{-\mathrm{SNR}/10}$, where SNR is the signal-to-noise ratio.

To determine whether a pixel within the detection domain is part of a scatterer, define an LSM indicator function for a pixel centered at $\bar{r}'_{n_d}$ as

$$I_\xi(\bar{r}'_{n_d}) = 10\log_{10}\sum_{m_e=1}^{M_e} \zeta_{m_e}\left|\xi(\bar{r}'_{n_d},\bar{r}_{m_e})\right|^2 \tag{9}$$

It is expected that the magnitude of $I_\xi(\bar{r}'_{n_d})$ for a pixel within a scatterer is much smaller than that outside of scatterers. This property will be used to train an U-Net to restore the object shape.

Recent researches on LSM have focused on improving the LSM indicator function [4, 7], to restore the object shape, under a specified threshold. In this work, deep learning method is used to train an U-Net with the LSM function in (9) as input, and no empirical threshold is required.

3. DEEP LEARNING LINEAR SAMPLING METHOD

Figure 1(b) shows the flowchart of the proposed deep learning linear sampling method (DLSM), which takes the distribution of LSM indicator in the detection domain to restore the object shape. In the training phase, the scattered fields at all the receivers from a training object sample are used to compute an LSM indicator (I_ξ) distribution, which is input to the U-Net to estimate an object shape, $\tilde{S}(\bar{r}')$. The weighting coefficients of the U-Net are fine-tuned by minimizing a loss function, which is the difference between cross entropies of the estimated object shape $\tilde{S}(\bar{r}')$ and the input object shape $S(\bar{r}')$.

U-Net has proven its effectiveness in biomedical image segmentation [14, 21] and permittivity estimation [13]. In this work, the LSM indicator distribution is treated as a 2D image. Fig. 2 shows the configuration of U-Net adopted in this work, where convp-n ($m \times 3 \times 3$) is a convolution layer with m input feature maps and n filters of size 3×3, MP (2×2) is a 2×2 max-pooling layer, upconvp-n ($m \times 3 \times 3$) is an up-convolution layer with m input feature maps and n filters of size 3×3, concat ($m + n$) is the concatenation of n feature maps from the previous layer and a skip connection of m feature maps from another layer, forming $m + n$ feature maps to be input to the next layer, and FC ($64 \times 1 \times 1$) is a fully connected layer before the output layer. The concat ($m+n$) is used to compensate for the blurring effect near object boundary after convolution layer [14].

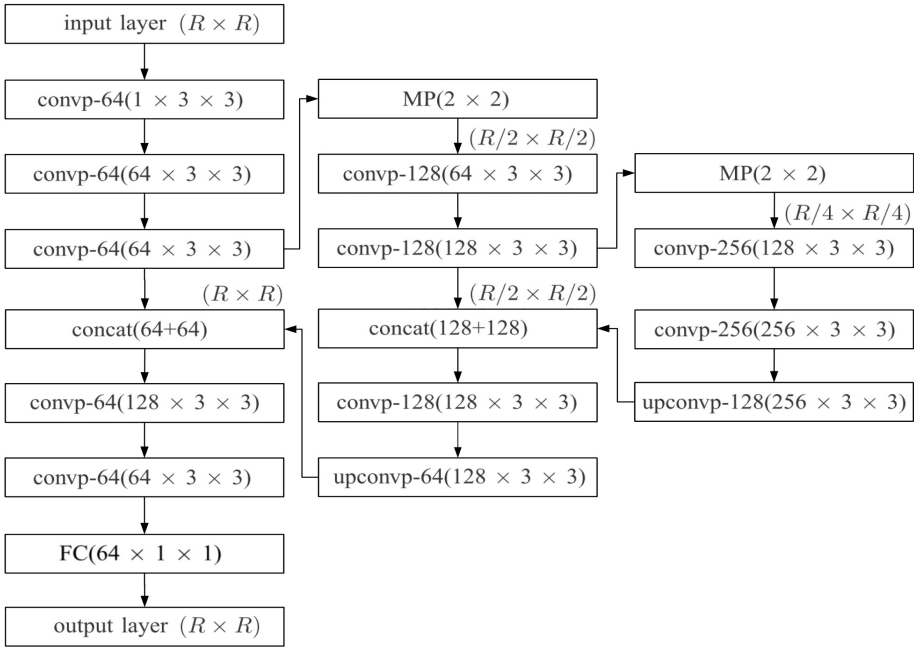

Figure 2. Configuration of U-Net adopted in this work.

The cross entropy, which has been widely used in segmentation problems, is given by [14, 21, 22]

$$L = -\sum_{n=1}^{N_d} s_n \log_{10} p_n \tag{10}$$

where $s_n = 1$ if pixel n belongs in the object and $s_n = 0$ otherwise, and p_n is the output of softmax. The softmax normalizes the exponential of its input vector to have unity norm in its output vector. The weight of the most probable solution is enhanced and the output vector takes the form of probability distribution, compatible to the definition of cross entropy in (10).

In the testing phase, the LSM indicator distributions of testing object samples are input to the U-Net, then the output is used to evaluate the performance of the trained U-Net. The whole process does not require any empirical threshold as in conventional LSMs.

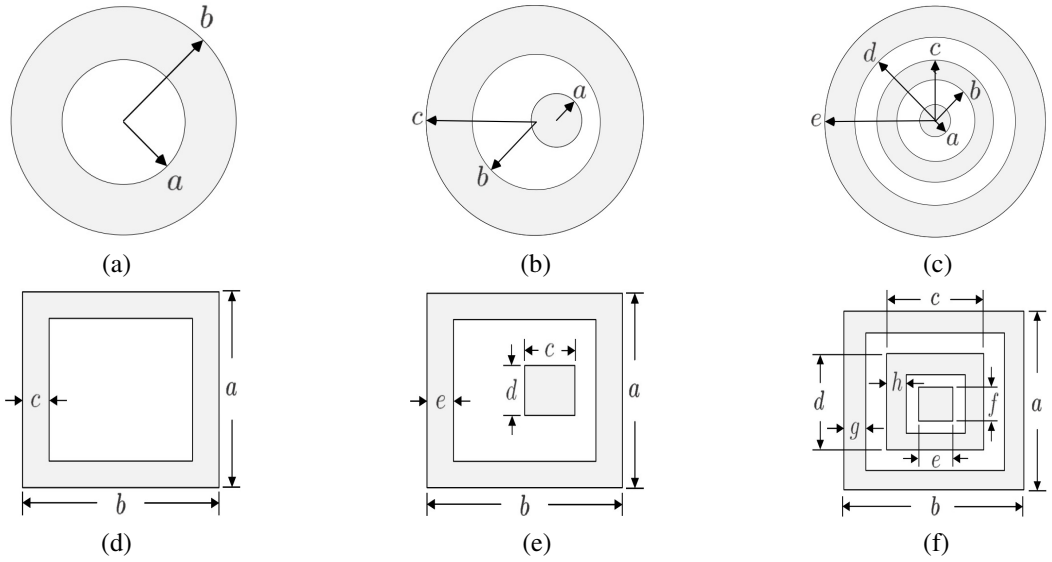

Figure 3. Geometries and parameters of training and testing samples, (a) circular ring, (b) circle inside circular ring, (c) circle inside two concentric rings, (d) rectangular ring, (e) rectangle inside rectangular ring, (f) rectangle inside two rectangular rings.

4. TRAINING DATA SET AND PERFORMANCE INDICES

Due to the non-uniqueness nature of inverse problems, a rectangular object was often restored to have rounded edges, and the gap between an object and its enclosing ring was often missing in the restored image. The proposed DLSM turns out to be able to overcome these difficulties. Fig. 3 shows six different types of training and testing samples used in this work, including rectangular and circular objects, bared or enclosed with one or two rings. Table 1 lists the ranges of geometrical parameters marked in Fig. 3. The parameters of each sample are randomly chosen from these specified ranges, the center piece and the rings are not allowed to touch or overlap with one another. The relative permittivity in each piece of a sample is randomly picked from the interval of [1, 5]. The background of the detection domain is assumed to be free space.

Table 1. Ranges of geometrical parameters.

shape	(a)	(b)	(c)	(d)	(e)	(f)
a (m)	0.125–0.5	0.3125–0.4375	0.125–0.625	0.25–1	0.65–1.125	1–1.75
b (m)	0.1875–0.5625	0.3125–0.5	0.2185–0.6875	0.25–1	0.65–1.125	1–1.75
c (m)	-	0.375–0.625	0.3125–0.75	0.0625–0.4375	0.525–1	0.90625–1.65625
d (m)	-	-	0.40625–0.8125	-	0.0625–0.5	0.90625–1.65625
e (m)	-	-	0.5–0.875	-	-	0.8125–1.525
f (m)	-	-	-	-	-	0.8125–1.525
g (m)	-	-	-	-	-	0.0625–0.8125
h (m)	-	-	-	-	-	0.0625–0.71875

To evaluate the fidelity of shape restoration, a total error index I_t is defined over the whole detection domain as [7]

$$I_t = 100 \times \frac{1}{N_d} \sum_{n=1}^{N_d} |s_n - \tilde{s}_n| \,(\%) \tag{11}$$

where s_n and $\tilde{s}_n$ are the true value and estimated value, respectively; $s_n = 1$ if the nth pixel belongs in the object and $s_n = 0$ otherwise. A spill-over index I_s is defined to count for misclassified pixels exterior to an object as

$$I_s = 100 \times \frac{1}{N_{st}} \sum_{n=1}^{N_{st}} |s_n - \tilde{s}_n| \,(\%) \tag{12}$$

where N_{st} is the total number of pixels exterior to an object. A material index I_m is defined to count for the filled pixels interior to an object as

$$I_m = 100 \times \frac{1}{N_{mt}} \sum_{n=1}^{N_{mt}} |s_n - \tilde{s}_n| \,(\%) \tag{13}$$

where N_{mt} is the total number of filled pixels interior to an object. Finally, a gap index I_g is defined to count for the blank pixels interior to an object as

$$I_g = 100 \times \frac{1}{N_{gt}} \sum_{n=1}^{N_{gt}} |s_n - \tilde{s}_n| \,(\%) \tag{14}$$

where N_{gt} is the total number of blank pixels interior to an object.

5. SIMULATIONS AND DISCUSSIONS

In this section, the size of detection domain shown in Fig. 1(a) is set to 2 m × 2 m and is divided into 64 × 64 uniform pixels. The operating frequency is set to 400 MHz, and 16 exciting probes and 32 receiving probes are placed at uniform spacing on the circular perimeter C_0, with radius of 3 m. The training data set contains six types of objects, as specified in Fig. 3, with 200 samples in each type. An object is considered as a strong scatterer if its contrast function defined in (2) times its size in wavelengths is greater than one [2, 23].

Most samples in Figs. 3(c) and 3(f) have radius close to one wavelength, and within each type of the training data set, 100 samples have relative permittivity in [1, 1.5], and the other 100 samples have relative permittivity (of at least one component) in [1.5, 5]. The testing data set contains the same six types of objects, with 50 samples in each type. In each type of the testing data set, 20 samples have relative permittivity in [1, 1.5], and the other 30 samples have relative permittivity (of at least one component) in [1.5, 5].

Then, the U-Net is trained in 600 epochs [24]. To facilitate convergence of the training phase, the learning rate is set to 10^{-7} in the first 200 epochs, 10^{-9} in the subsequent 200 epochs, and 10^{-11} in the last 200 epochs [22]. The momentum is set to 0.99 to adjust the change of weight in each layer between two consecutive iterations [22]. MatConvNet toolbox [22] is used to train the U-Net, on a personal computer with 3.6 GHz Intel Core i7-9700KF CPU and 32 GB RAM. Each epoch takes about 2 CPU minutes, which can be significantly reduced by using GPU parallelization [13, 22].

For comparison, the empirical threshold required in conventional threshold method is determined as [4]

$$v_{\text{th}} = \min\{I_\xi\} + \gamma \left(\max\{I_\xi\} - \min\{I_\xi\}\right) \tag{15}$$

with $\gamma = 0.5$ [7].

5.1. Test on Nested Circles

First input the 50 testing samples of circular ring to the trained U-Net, one at a time. The four indices defined in (11)–(14) are applied to the output of each sample. Fig. 4 shows the images of four restored samples, with their I_t at the percentiles of 10, 30, 50, and 90, respectively.

The LSM indicator in the second row reveals some sketchy ring shape, which looks closer to the true shape when the relative permittivity is low. The conventional threshold method restores a solid circular shape in these four samples, suggesting that the results are sensitive to a proper empirical

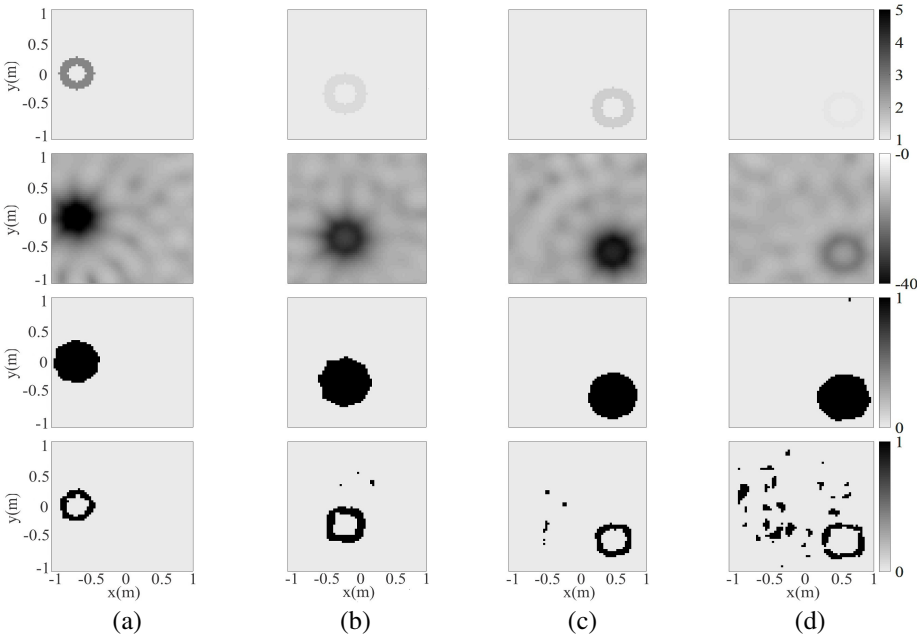

Figure 4. Restored samples of circular ring at I_t percentile of (a) 10, (b) 30, (c) 50, (d) 90; SNR = 20 dB, first row: true relative permittivity, second row: LSM indicator, third row: threshold method, fourth row: DLSM.

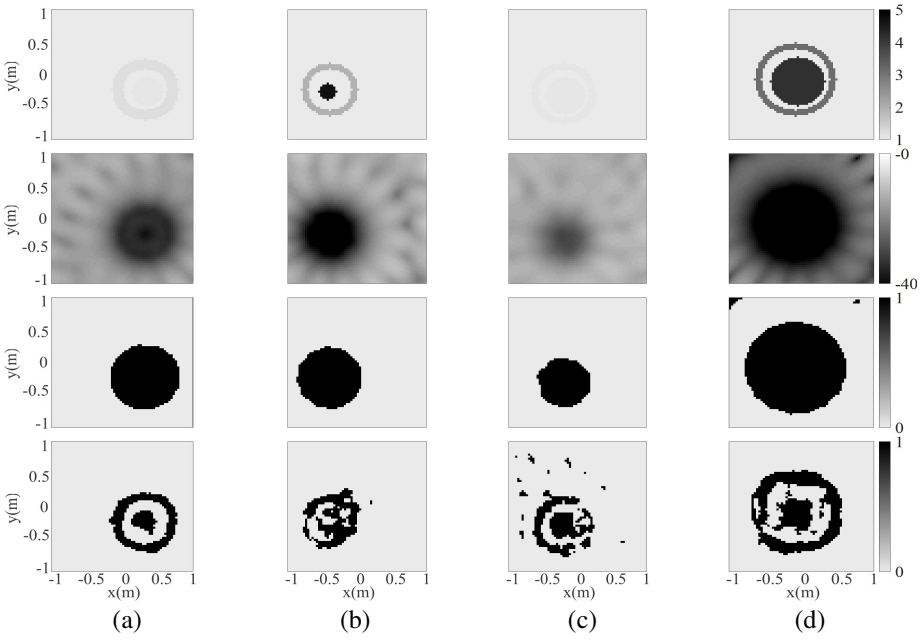

Figure 5. Restored samples of circle inside circular ring at I_t percentile of (a) 10, (b) 30, (c) 50, (d) 90; SNR = 20 dB, first row: true relative permittivity, second row: LSM indicator, third row: threshold method, fourth row: DLSM.

threshold. On the other hand, the DLSM can faithfully restore a circular ring, with some speckles on the background.

Figure 5 shows the images of four restored samples of circle inside circular ring, with their I_t at the percentiles of 10, 30, 50, and 90, respectively. The LSM indicator in the second row of Fig. 5(a) reveals features of the object shape, but the other three in the second row look like a solid circle, with

the outer ring merging with the inside circle. The threshold method restores these samples as solid circles without gap in between. The shapes restored with the DLSM are discernible, with some samples displaying voids in the ring, crack in the circle and speckles in the background. There are two possible causes for these artifacts. First, the training samples contain no noise, hence testing samples with noise may arouse some artifacts. Second, increasing the number of training samples may help reduce these artifacts.

Figure 6 shows the images of four restored samples of circle inside two concentric rings, at the same I_t percentiles as in the previous two cases. The LSM indicator in the second row of Figs. 6(b) and 6(c) portray a circle smaller than the true object, possibly because the outermost ring has higher permittivity and ring width, blocking the scattered field from the inner circle. The threshold method seems to work for sample in Fig. 6(b), but misses the gaps in the other three samples. Similar results were observed in [2], suggesting that conventional LSM may not work well in restoring strong scatterers. On the other hand, the DLSM can restore the first three samples clearly. The three parts in the fourth sample are partially connected, but each part is still discernible.

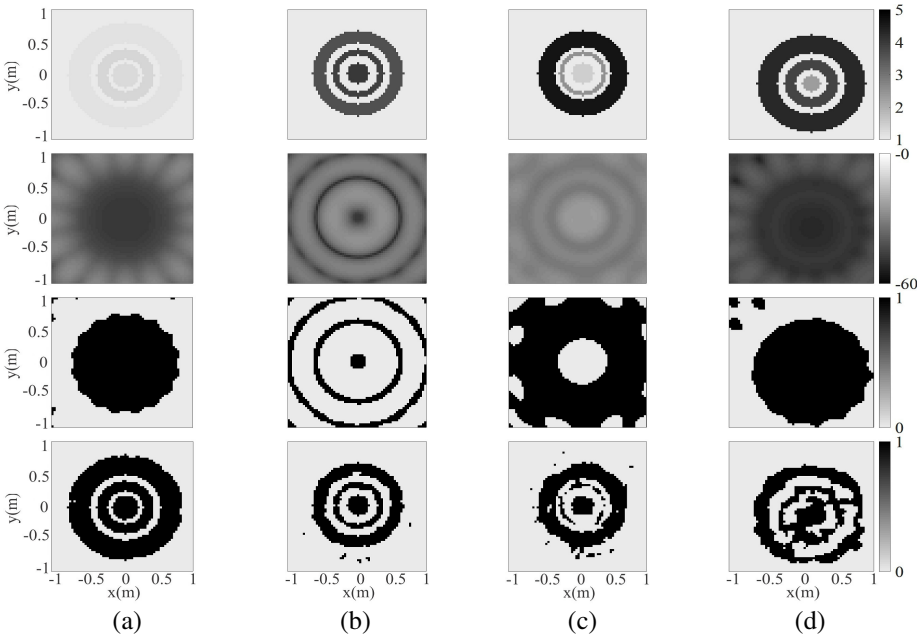

Figure 6. Restored samples of circle inside two concentric rings at I_t percentile of (a) 10, (b) 30, (c) 50, (d) 90; SNR = 20 dB, first row: true relative permittivity, second row: LSM indicator, third row: threshold method, fourth row: DLSM.

Figure 7 shows the cumulative distributions of the four performance indices associated with circular ring (shape c1), circle inside circular ring (shape c2) and circle inside two concentric rings (shape c3), respectively. Among the testing samples of circular ring, 95% of them have $I_t < 10\%$ and 75% of them have $I_t < 5\%$. The I_t index of shape c3 after 80th percentile becomes higher than those of shapes c1 and c2, which is consistent with the observation that the worst restored shapes of more complicated geometry become more fragmented as shown in the fourth row of Fig. 6(d).

The spill-over index of all the three shapes is insignificant before the 50th percentile. The material index $I_m < 30\%$ for about 80% of shapes c1 or c3, and 50% of shape c2. The I_g index in the first 40 percentiles of samples with shapes c1 and c3 is negligible, which confirms the efficacy of the DLSM in restoring the blank space interior to a layered object.

5.2. Test on Nested Rectangles

Figure 8 shows the images of four testing samples of rectangular ring at the I_t percentiles of 10, 30, 50, and 90, respectively. The images in the third row acquired with the threshold method resemble their

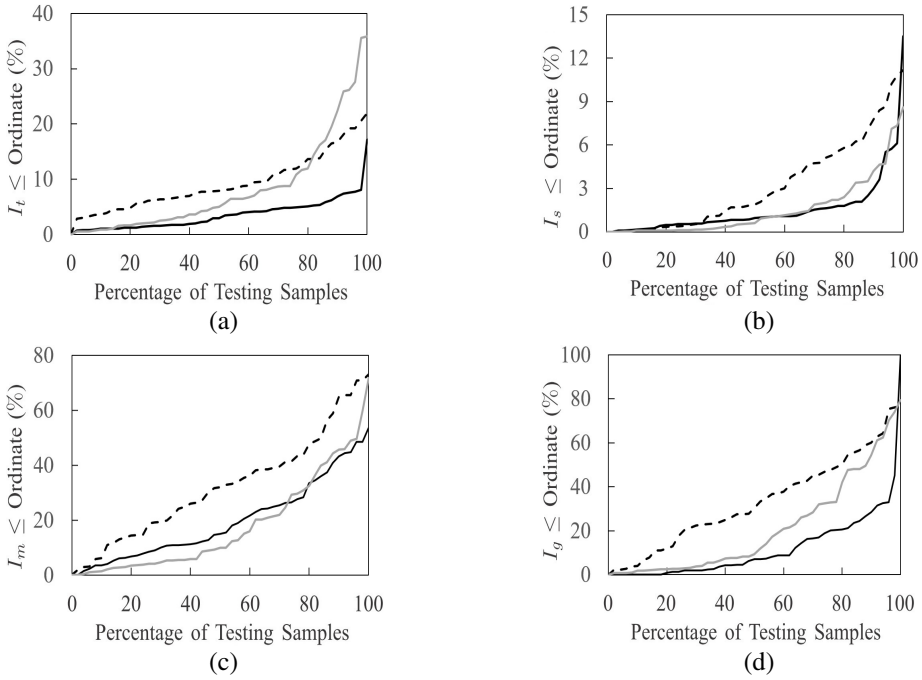

Figure 7. Cumulative distribution of (a) I_t, (b) I_s, (c) I_m, (d) I_g; ———: circular ring, − − −: circle inside circular ring, ———: circle inside two concentric rings.

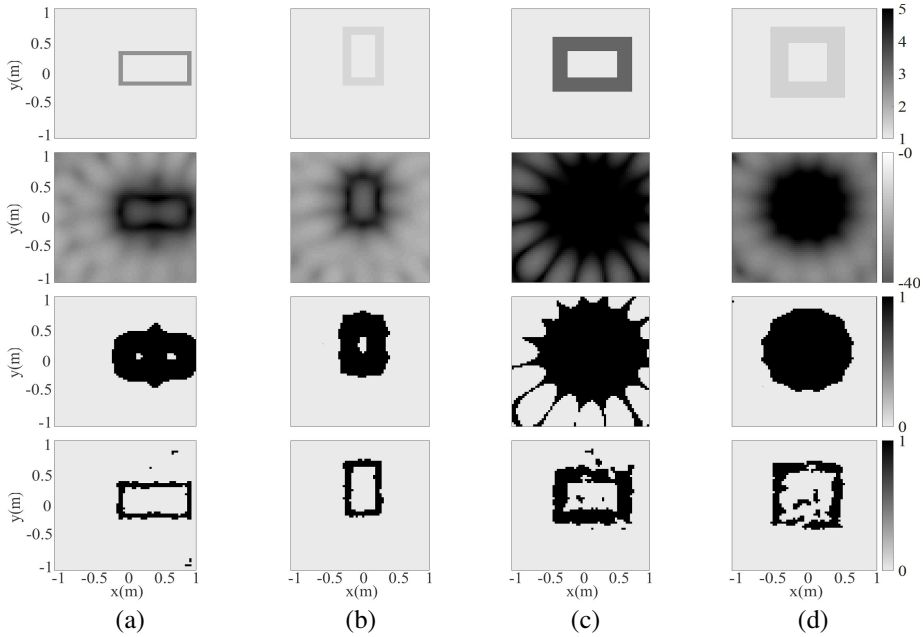

Figure 8. Restored samples of rectangular ring at I_t percentile of (a) 10, (b) 30, (c) 50, (d) 90; SNR = 20 dB, first row: true relative permittivity, second row: LSM indicator, third row: threshold method, fourth row: DLSM.

counterpart LSM indicator distributions in the second row. The sharp corners are severely rounded in samples (a) and (b), and a vertical stub appears in the middle of sample (a). The restored images take solid circular shape in samples (c) and (d). The restored shape in sample (c) is severely distorted possibly because the ring with large relative permittivity prevents the incident wave from penetrating it.

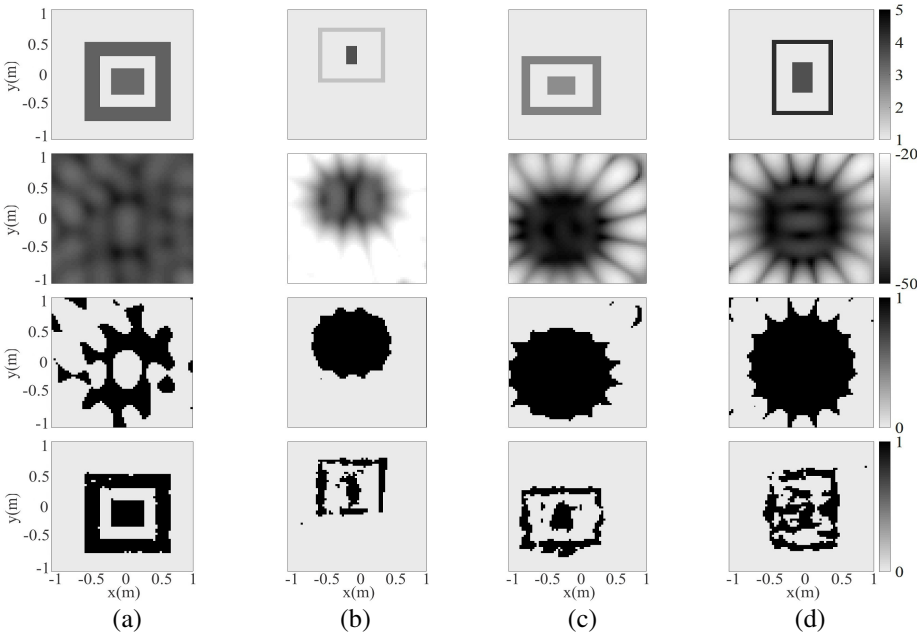

Figure 9. Restored samples of rectangle inside rectangular ring at I_t percentile of (a) 10, (b) 30, (c) 50, (d) 90; SNR = 20 dB, first row: true relative permittivity, second row: LSM indicator, third row: threshold method, fourth row: DLSM.

On the other hand, the acquired images of samples (a) and (b) with the DLSM preserve sharp corners of rectangle without cracks, and some speckles and cracks appear in the images of samples (c) and (d).

Figure 9 shows the images of four restored samples of rectangle inside rectangular ring at the same I_t percentiles as in the previous case. The LSM indicator distributions display hub-radiant spike features but do not clearly show the inner rectangle, except in sample (b), which possesses a narrow ring with lower relative permittivity. The ring in sample (a) has higher permittivity, which prevents the incident waves from penetrating it. In contrast, the image of sample (a) acquired with the DLSM faithfully restore the original shape. The images of samples (b), (c) and (d) are significantly smeared, but the features of rectangle and rectangular ring are recognizable. Fig. 10 shows the images of four restored samples of rectangle inside two rectangular rings, at the same I_t percentiles as in the previous cases. For samples (a) and (b), with lower permittivity, their LSM indicator distributions reveal the central rectangle, but the three components are clumped into one chunk in the images acquired with the threshold method. For sample (c), higher permittivity of the outer ring prevents the incident waves from probing the interior rectangle, as shown in its LSM indicator distribution and the acquired image with the threshold method. In contrast, lower permittivity of the outer ring in sample (d) allows the incident waves to probe the interior rectangle, as shown in its LSM indicator distribution and the acquired image with the threshold method.

The DLSM cannot restore the shapes as neatly as in the last two figures. The basic skeleton can be recognized, with many additional cracks and speckles.

Figure 11 shows the cumulative distributions of the four performance indices associated with rectangular ring (shape r1), rectangle inside rectangular ring (shape r2) and rectangle inside two rectangular rings (shape r3), respectively. Among the testing samples of shape r1, 90% of them have $I_t < 10\%$ and 70% of them have $I_t < 5\%$. The I_t index of shape r3 is significantly higher than those of shapes r1 and r2 due to the more complicated geometry of the former. The spill-over index of all the three shapes is insignificant in the first 30 percentiles of samples.

The material index of shapes r1 and r2 is $I_m < 20\%$ for about 50% of the samples, and $I_m < 50\%$ for about 50% of the samples in shape r3. The I_g index is negligible in the first 40 percentiles of shape r1, and the first 20 percentiles of shape r2. All these indices suggest that samples of shape r3 are more difficult to restore than those of shapes r1 and r2. The samples which are not well restored with the

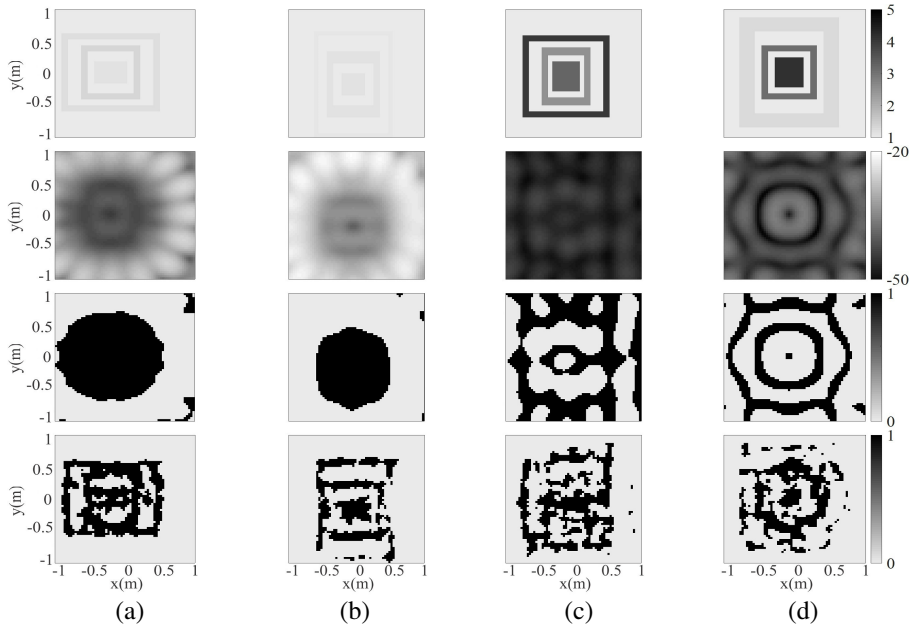

Figure 10. Restored samples of rectangle inside two rectangular rings at I_t percentile of (a) 10, (b) 30, (c) 50, (d) 90; SNR = 20 dB, first row: true relative permittivity, second row: LSM indicator, third row: threshold method, fourth row: DLSM.

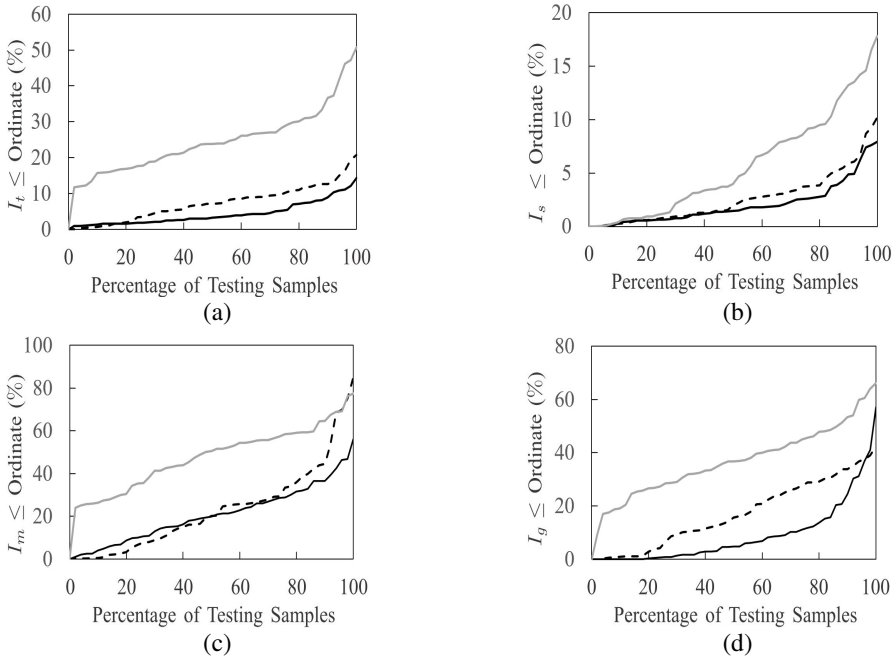

Figure 11. Cumulative distribution of (a) I_t, (b) I_s, (c) I_m, (d) I_g; ———: rectangular ring, – – –: rectangle inside rectangular ring, ———: rectangle inside two rectangular rings.

threshold method also cast large indices when restored with the DLSM.

In summary, the DLSM has been demonstrated to effectively restore the shapes of circular and rectangular layered objects, which are more complicated than those presented in the literature, especially when interior gaps are included. Some geometrical features that cannot be faithfully restored with conventional threshold method can be better restored with the proposed DLSM.

5.3. Test on Austria Profile

Figure 12 shows a testing sample of Austria profile with relative permittivity equal 1.5, which is not included in the training dataset. Some geometrical features are revealed in the LSM indicator and the acquired image with the DLSM, but the fidelity to the true shape can be subjective. The I_t indices of threshold method and DLSM are 19% and 15.4%, respectively. The proposed method has the performance matches that of conventional LSM, even when the shape is not included in the training data set.

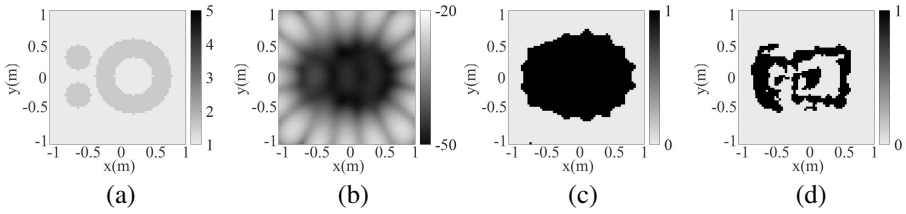

Figure 12. Restored Austria profile, SNR = 20 dB, (a) true permittivity, (b) LSM indicator, (c) threshold method, (d) DLSM.

6. CONCLUSIONS

A DLSM is proposed by integrating a CNN type of U-Net and LSM to restore the shape of 2D layered objects embedding interior gaps, without requiring any empirical threshold. Four performance indices are defined to compare the restored shape to the original shape of object. The simulation results of conventional LSM threshold method are compared. The pixelwise error of the DLSM is much lower than that of the threshold method. The DLSM can restore the gaps interior to layered objects more accurately and can distinguish rounded corners from sharp corners.

REFERENCES

1. Bevacqua, M. and T. Isernia, "Shape reconstruction via equivalence principles, constrained inverse source problems and sparsity promotion," *Progress In Electromagnetics Research*, Vol. 158, 37–48, 2017.
2. Bevacqua, M. T. and R. Palmeri, "Qualitative methods for the inverse obstacle problem: A comparison of experimental data," *J. Imaging*, Vol. 5, No. 4, 47, Apr. 2019.
3. Shao, W. and Y. Du, "Microwave imaging by deep learning network: Feasibility and training method," *IEEE Trans. Antennas Propagat.*, Vol. 68, No. 7, 5626–5634, Jul. 2020.
4. Agarwal, K., X. Chen, and Y. Zhong, "A multipole-expansion based linear sampling method for solving inverse scattering problems," *Optics Express*, Vol. 18, No. 6, 6366–6381, 2010.
5. Cakoni, F., D. Colton, and P. Monk, *The Linear Sampling Method in Inverse Electromagnetic Scattering*, SIAM Press, 2011.
6. Catapano, I., L. Crocco, and T. Isernia, "On simple methods for shape reconstruction of unknown scatterers," *IEEE Trans. Antennas Propagat.*, Vol. 55, No. 5, 1431–1436, May 2007.
7. Burfeindt, M. J. and H. F. Alqadah, "Qualitative inverse scattering for sparse-aperture data collections using a phase-delay frequency variation constraint," *IEEE Trans. Antennas Propagat.*, Vol. 68, No. 4, 7530–7540, Nov. 2020.
8. Potthast, R., "A study on orthogonality sampling," *Inverse Problem*, Vol. 26, No. 7, 074015, 2010.
9. Bevacqua, M. T., T. Isernia, R. Palmeri, M. N. Akinci, and L. Crocco, "Physical insight unveils new imaging capabilities of orthogonality sampling method," *IEEE Trans. Antennas Propagat.*, Vol. 68, No. 5, 4014–4021, May 2020.
10. Li, J. Z., H. Y. Liu, and J. Zou, "Strengthened linear sampling method with a reference ball," *SIAM J. Sci. Comput.*, Vol. 31, 4013–4040, 2009.

11. Crocco, L., L. D. Donato, I. Catapano, and T. Isernia, "An improved simple method for imaging the shape of complex targets," *IEEE Trans. Antennas Propagat.*, Vol. 61, No. 2, 843–851, Feb. 2013.
12. Guo, R., Z. Jia, X. Song, M. Li, F. Yang, S. Xu, and A. Abubakar, "Pixel-and model-based microwave inversion with supervised descent method for dielectric targets," *IEEE Trans. Antennas Propagat.*, Vol. 68, No. 12, 8114–8126, Jun. 2020.
13. Wei, Z. and X. D. Chen, "Deep-learning schemes for full-wave nonlinear inverse scattering problems," *IEEE Trans. Geosci. Remote Sensing*, Vol. 57, No. 4, 1849–1860, Apr. 2019.
14. Ronneberger, O., P. Fischer, and T. Brox, "U-net: Convolutional networks for biomedical image segmentation," *Medical Image Computing and Computer-Assisted Intervention (MICCAI)*, 234–241, 2015.
15. Khoshdel, V., A. Ashraf, and J. LoVetri, "Enhancement of multimodal microwave-ultrasound breast imaging using a deep-learning technique," *Sensors*, Vol. 19, No. 18, 4050, 2019.
16. Yao, H. M., W. E. I. Sha, and L. Jiang, "Two-step enhanced deep learning approach for electromagnetic inverse scattering problems," *IEEE Antennas Wireless Propagat. Lett.*, Vol. 18, No. 11, 2254–2258, Jan. 2019.
17. Sanghvi, Y., Y. Kalepu, and U. K. Khankhoje, "Embedding deep learning in inverse scattering problems," *IEEE Trans. Comput. Imag.*, Vol. 6, 46–56, Jul. 2020.
18. Yago, A., M. Cavagnaro, and L. Crocco, "Deep learning-enhanced qualitative microwave imaging: Rationale and initial assessment," *EuCAP*, 1–5, Dusseldorf, Germany, Mar. 2021.
19. Crocco, L., I. Catapano, L. D. Donato, and T. Isernia, "The linear sampling method as a way to quantitative inverse scattering," *IEEE Trans. Antennas Propagat.*, Vol. 60, No. 4, 1844–1853, Apr. 2012.
20. Colton, D., H. Haddar, and M. Piana, "The linear sampling method in inverse electromagnetic scattering theory," *Inverse Problem*, Vol. 19, 105–137, 2003.
21. Alom, M. Z., M. Hasan, C. Yakopcic, T. M. Taha, and V. K. Asari, "Recurrent residual convolutional neural network based on U-Net (R2U-Net) for medical image segmentation," arXiv 1802.06955, 2018.
22. Kim, P., *MATLAB Deep Learning with Machine Learning, Neural Networks and Artificial Intelligence*, APress, 2017.
23. Xu, K., L. Wu, X. Ye, and X. Chen, "Deep learning-based inversion methods for solving inverse scattering problems with phaseless data," *IEEE Trans. Antennas Propagat.*, Vol. 68, No. 11, 7457–7470, Nov. 2020.
24. Vedaldi, A., K. Lenc, and A. Gupta, "MatConvNet: Convolutional neural networks for MATLAB," *ACM Int. Conf. Multimedia*, 689–692, 2015.